University of Wollongong
Research Online

Australian Institute for Innovative Materials - Papers

Australian Institute for Innovative Materials

1-1-2020

Comparative evaluation of the structural and other features governing photo-electrochemical oxygen evolution by Ca/Mn oxides

Ankita Gagrani

Mohammed Alsultan
University of Wollongong, mfka287@uowmail.edu.au

Gerhard F. Swiegers
University of Wollongong, swiegers@uow.edu.au

Takuya Tsuzuki

Follow this and additional works at: https://ro.uow.edu.au/aiimpapers

 Part of the Engineering Commons, and the Physical Sciences and Mathematics Commons

Recommended Citation

Gagrani, Ankita; Alsultan, Mohammed; Swiegers, Gerhard F.; and Tsuzuki, Takuya, "Comparative evaluation of the structural and other features governing photo-electrochemical oxygen evolution by Ca/Mn oxides" (2020). *Australian Institute for Innovative Materials - Papers*. 4102.
https://ro.uow.edu.au/aiimpapers/4102

Research Online is the open access institutional repository for the University of Wollongong. For further information contact the UOW Library: research-pubs@uow.edu.au

Comparative evaluation of the structural and other features governing photo-electrochemical oxygen evolution by Ca/Mn oxides

Abstract

Mn-Based oxides, particularly CaMn oxides, have recently attracted significant practical interest as a new class of catalyst due to their elemental and structural similarity to the natural oxygen evolving cluster (OEC) in photosynthetic plant cells. However, their performance as oxygen-generating anodes in photoelectrochemical cells has not been studied in detail. In this work, ultra-fine particles of amorphous MnO2, crystalline MnO2 nanorods, Ca2Mn3O8, CaMn2O4 and CaMnO3 were synthesised using a green and scalable mechanochemical method. The particles were comparatively studied as water oxidation photocatalysts in a photo-electrochemical cell at near-neutral pH. The oxides were immobilized on the anode surface using an organic, conducting polymer that facilitated electron exchange and catalytic turnover in a manner similar to redox-active tyrosine in the OEC. The differences in their photocatalytic performances were evaluated in terms of: (1) structural similarities to the natural OEC, (2) Mn oxidation state, (3) crystal structure, (4) specific surface area, (5) electron energy state, and (6) the presence/absence of Ca. The results confirmed the importance of having a local structure that is as similar as possible to the natural OEC cluster, including the presence of Ca. However, it also indicated that it is simplistic to focus only on this feature. The other factors listed above may also play a critical role in performance. Future design of biomimetic catalysts for solar fuel production needs to consider and concurrently optimize all of the relevant influences.

Keywords

features, governing, photo-electrochemical, oxides, oxygen, comparative, other, evolution, structural, ca/mn, evaluation

Disciplines

Engineering | Physical Sciences and Mathematics

Publication Details

Gagrani, A., Alsultan, M., Swiegers, G. F. & Tsuzuki, T. (2020). Comparative evaluation of the structural and other features governing photo-electrochemical oxygen evolution by Ca/Mn oxides. Catalysis Science & Technology, (7), 2152.

This journal article is available at Research Online: https://ro.uow.edu.au/aiimpapers/4102

ARTICLE

Comparative evaluation of the structural and other features governing photo-electrochemical oxygen evolution by Ca/Mn oxides

Received 00th January 20xx,
Accepted 00th January 20xx

DOI: 10.1039/x0xx00000x

Ankita Gagrani,[a] Mohammed Alsultan [b,c] Gerhard F. Swiegers *[b] and Takuya Tsuzuki*[a]

Mn-based oxides, particularly CaMn oxides, have recently attracted significant practical interest as a new class of catalyst due to their elemental and structural similarity to the natural oxygen evolving cluster (OEC) in photosynthetic plant cells. However, their performance as oxygen-generating anodes in photoelectrochemical cells has not been studied in detail. In this work, ultra-fine particles of amorphous MnO_2, crystalline MnO_2 nanorods, $Ca_2Mn_3O_8$, $CaMn_2O_4$ and $CaMnO_3$ were synthesised using a green and scalable mechanochemical method. The particles were comparatively studied as water oxidation photocatalysts in a photo-electrochemical cell at near-neutral pH. The oxides were immobilized on the anode surface using an organic, conducting polymer that facilitated electron exchange and catalytic turnover in a manner similar to redox-active tyrosine in the OEC. The differences in their photocatalytic performances were evaluated in terms of: (1) structural similarities to the natural OEC, (2) Mn oxidation state, (3) crystal structure, (4) specific surface area, (5) electron energy state, and (6) the presence/absence of Ca. The results confirmed the importance of having a local structure that is as similar as possible to the natural OEC cluster, including the presence of Ca. However, it also indicated that it is simplistic to focus only on this feature. The other factors listed above may also play a critical role in performance. Future design of biomimetic catalysts for solar fuel production needs to consider and concurrently optimize all of the relevant influences.

Introduction

Photosynthesis, nature's solar technology, is the most efficient water-splitting system known to date. $CaMn_4O_5$ clusters within the Photosystem-II (PSII) proteins in plant cells, have been identified as the key structural component for splitting water using sunlight during photosynthesis.[1] The natural oxygen evolving cluster (OEC) has an asymmetric, cubane-like structure that resembles a distorted chair (Fig. 1).[2] In the cubane, a Ca and three Mn ions form four corners with the remaining four corners occupied by four O atoms. A fourth, dangling Mn ion is outside the cubane and is linked to the cluster via a corner Mn, a corner O and a di-μ-oxo bridge. Catalytic turnover occurs by electron exchange with a tyrosine residue that is closely proximate to the OEC.

Recent computational studies showed that two water molecules are bound to the Ca and dangling Mn atoms and play a key role in the water-splitting process; thus, the atomic arrangement of the Mn_4Ca cubane is thought to be critical to natural water splitting.[3] This discovery inspired scientists to investigate the synthesis and water-splitting capabilities of several manganese-based oxides, in particular calcium manganese oxides, in order to artificially split water using solar energy to produce a clean fuel, hydrogen.[4]

For example, Baktash *et al.* reported the synthesis and chemical water oxidation of porous CaMn oxides with a unique foam-like nanostructure.[5] They concluded that the catalytic activity was affected by the atomic arrangement and structural order within the CaMn oxides.[5] Frey *et al.* investigated the water oxidation properties of a series of Ca birnessite powders and found that their water-oxidation rates are affected by the Ca : Mn ratio.[6] Najafpour showed that, when the CaMn oxides are structurally similar to the natural OEC, they tend to exhibit strong water oxidation ability.[7] Although these studies produced significant insights into the redox properties of calcium-manganese oxides, the studies were conducted

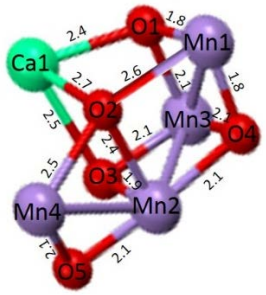

Fig. 1 Structure of the Mn_4CaO_5 cluster in the natural oxygen evolving cluster (OEC). Inter-atomic distances are indicated in Å. Ca is shown in green, Mn in blue, and O in red.

[a] *Research School of Electrical, Energy and Materials Engineering, The Australian National University, Canberra, ACT 2601, Australia.*
E-mail: takuya.tsuzuki@anu.edu.au; Tel: +61 2 6125 9296
[b] *Intelligent Polymer Research Institute, University of Wollongong, Wollongong, NSW 2522, Australia.*
E-mail: swiegers@uow.edu.au
[c] *Department of Science, College of Basic Education, University of Mosul, Mosul 41002, Iraq.*

Please do not adjust margins

without light irradiation. In artificial photosynthesis, it is self-evident that light illumination is very important.

Najafpour et al. reported light-driven water oxidation with several Mn and CaMn compounds such as MnO_2, $Ca_2Mn_3O_8$, $CaMnO_3$, $CaMn_2O_4$, but only in the presence of various sacrificial reagents.[7] Sacrificial oxidants, in particular Ce^{4+}, limit the useful operating pH and may over-estimate photocatalytic activities, due to their high oxidation power.[8] Only one paper has reported the photocatalytic water splitting properties of Ca_xMnO_y as a sole catalyst, but the catalysts were tested in the form of free-standing nanoparticles.[9] For practical applications of artificial photosynthesis, it is crucial to immobilize the catalysts on conducting electrodes as an anode, instead of using the catalysts in a form of free powders. A small number of studies have been published on the catalytic properties of Ca_xMnO_y as electrode materials, but water splitting was induced only electrocatalytically without light irradiation.[10-14]As such, it is still not understood how Ca_xMnO_y systems would perform as water-oxidising catalysts when photochemical and electrochemical conditions are combined. In particular, the influence of non-structural features on catalytic performance has not been studied or evaluated. For example, while structural similarities to the natural OEC tend to amplify water oxidation ability,[7] CaMn oxides that are structurally dissimilar to the natural OEC, including $CaMnO_3$ and $CaMn_4O_8$, also show water oxidation catalytic abilities.[15-16] The correlation between structure and light-driven catalytic water-splitting properties has therefore not yet been elucidated. $CaMnO_3$, $Ca_2Mn_3O_8$ and $CaMn_2O_4$ have higher water oxidation efficiencies than MnO_2 in the presence of various sacrificial reagents without light irradiation.[15] However, little is known about light-driven water oxidation efficiencies of the immobilized CaMn oxides compared to MnO_2.

This manuscript reports a new study to address this research gap, by immobilizing $Ca_xM_nO_y$ catalysts within the anode of a photo-electrochemical cell and evaluating their photoelectric water oxidation performance, for the first time. We developed a new electrode design for Mn-based catalysts in photo-electrochemical cells, using polypyrrole, enabling increased charge separation efficiency within the anode and, in turn, improved oxygen evolution in the photo-electrochemical cell.

In this study, different Mn and CaMn oxides (amorphous MnO_2, crystalline MnO_2 nanorods, $Ca_2Mn_3O_8$, $CaMnO_3$ and $CaMn_2O_4$) have been comparatively studied as light-driven water oxidation catalysts within photo-anodes in photoelectrochemical cells. The influence of their structural similarity to the natural OEC cluster was quantitatively evaluated, along with the effect of Mn oxidation state, crystal structure, specific surface area, and the presence / absence of Ca. The results confirmed that structural similarity to the natural OEC, including the presence / absence of Ca, is an important factor in achieving high catalytic activities. However, the results also challenge the simplistic approach of focussing only on this feature. The study demonstrated that specific surface area and Mn oxidation state are also important, albeit that their relative influence could not be conclusively established.

In order to achieve high catalytic efficiency, materials with a large surface area and small particle sizes are preferred, as they provide more catalytically active sites.[4] However, green and scalable synthesis techniques of ultrafine calcium manganese oxides have seen little advancement to date. In addition, previously reported synthesis methods of calcium manganese oxides used organic solutions, which can pose environmental and health risks.[4] As such, the development of solvent-free chemical processes is imperative for commercial applications of calcium manganese oxides. Therefore, it is important to develop a solvent free, economical and scalable method for the synthesis of calcium manganese oxide nanocatalyst. In this study, calcium manganese oxide ultrafine particles were synthesised using a scalable and environmentally advantageous technique, mechanochemical processing[17], and their photo-electrochemical characteristics in water oxidation reactions was studied to elucidate the relation between the synthesis method and catalytic performance of the Ca/Mn oxides. All Mn compounds were immobilized on the photo-anodes by an organic, conducting polymer (polypyrrole, PPy). The CaMn oxides formed a type-II (staggered type) heterojunction with the PPy, enabling increased charge separation within the anode, which, in turn, improved oxygen evolution.

Experimental Procedure

Synthesis of amorphous and crystalline MnO_2

Amorphous MnO_2 nanoparticles were synthesized via the following solid-state redox reaction during mechanical milling:

$$2KMnO_4(s) + MnCl_2(s) + 10KCl(s) \rightarrow 3MnO_2(s) + 12KCl(s) + O_2(g) \quad (1)$$

The addition of excess KCl in the starting powder mixture prevented agglomeration of MnO_2 nanoparticles in the product phase. Crystalline MnO_2 nanorods were produced by heating the as-milled powder at 350 °C for 1 h in air. The as-milled powder was washed with Millipore Milli-Q ultrapure water multiple times to remove KCl and the remaining powder was dried in an oven at 50 °C for 9 h. The detailed synthesis procedure is described elsewhere.[17]

Synthesis of $Ca_2Mn_3O_8$

$Ca_2Mn_3(CO_3)_5$ nanoparticles were produced via the following reaction:

$$2\,CaCl_2(s) + 3\,MnCl_2(s) + 5\,K_2CO_3(s) + 29\,KCl(s) \rightarrow Ca_2Mn_3(CO_3)_5(s) + 39\,KCl(s) \quad (2)$$

and subsequent thermal decomposition of $Ca_2Mn_3(CO_3)_5$ into $Ca_2Mn_3O_8$. For initiating reaction (2), a stoichiometric amount of $MnCl_2$ (99.9% Sigma Aldrich, 0.996g) and $CaCl_2$ (>93%, granular, anhydrous, Sigma Aldrich, 0.586g) was agitated for 2 h using a SPEX 8000M mill. Then, K_2CO_3 (AnalaR NORMAPUR, VWR, 1.823 g) and KCl (AnalaR NORMAPUR, VWR, 5.8 g) were added along with hardened steel balls of 9.2 mm in diameter. A ball-to-powder mass ratio of 10:1 was used in the milling process. The mixture was milled in a hardened steel vial for 4 h

 This journal is © The Royal Society of Chemistry 20xx

Please do not adjust margins

Please do not adjust margins

in a SPEX 8000M mill to obtain $Ca_2Mn_3(CO_3)_5$ nanoparticles embedded in a KCl salt matrix. Addition of excess KCl salt in the starting powder mixture served as a physical barrier for the purpose of preventing agglomeration of $Ca_2Mn_3(CO_3)_5$ particles in the product phase. The as-milled $Ca_2Mn_3(CO_3)_5$ powders were heat treated at 600 °C for 1 h in air to decompose into $Ca_2Mn_3O_8$. The powder was then washed multiple times to remove KCl, with Millipore Milli-Q ultrapure water (18 MΩ cm) using an ultrasonic bath and a centrifuge. The remaining powder was collected and dried in an oven at 50 °C for several hours.

Synthesis of $CaMnO_3$ and $CaMn_2O_4$

$CaMnO_3$ and $CaMn_2O_4$ particles were synthesized using a similar methodology to the one used for the synthesis of $Ca_2Mn_3O_8$ nanoparticles. The following reactions were initiated in a SPEX mill to produce precursor nanoparticles, $CaMn_2(CO_3)_3$ and $CaMn(CO_3)_2$, respectively:

$$CaSO_4(s) + 2\ MnSO_4(s) + 3\ K_2CO_3(s) + 11\ K_2SO_4(s) \rightarrow CaMn_2(CO_3)_3(s) + 14\ K_2SO_4(s) \quad (3)$$

$$CaSO_4(s) + MnSO_4(s) + 2\ K_2CO_3(s) + 7\ K_2SO_4(s) \rightarrow CaMn(CO_3)_2(s) + 9\ K_2SO_4(s) \quad (4)$$

The reason for using sulfate salts in these reactions instead of chloride salts, was the higher melting point of K_2SO_4 (1,069 °C) in comparison to KCl (770 °C). A salt with a higher melting point was required to form $CaMn_2O_4$ and $CaMnO_3$ because the thermal decomposition of $CaMn_2(CO_3)_3$ and $CaMn(CO_3)_2$ occurs at a temperature higher than 770 °C, and it is crucial for the salt matrix to stay in a solid form during heat treatment to prevent particle agglomeration.

$MnSO_4$ was obtained by dehydrating the as-received $MnSO_4{\cdot}4H_2O$ (99%, Sigma Aldrich) according to the procedure described by Sinha *et al*.[18] All other chemicals were used without further purification. First, a stoichiometric amount of $CaSO_4$ (anhydrous, 99%, Alfa Aesar) and $MnSO_4$ was agitated for 2 h, followed by the addition of K_2CO_3 (AnalaR NORMAPUR, VWR) and K_2SO_4 (ACS, 99.0% min, Alfa Aesar). The mixture was ball-milled for 4 h with a ball-to-powder mass ratio of 10:1, in a Spex 8000M mill. The as-milled powder was subjected to heat treatment at 800 °C for 3 h, and 950 °C for 1 h for obtaining $CaMnO_3$ and $CaMn_2O_4$, respectively. Subsequently the powder was washed with DI water and dried.

Physical Characterisation

The crystal structure of the catalyst powders was examined at room temperature using a D2 Phaser X-ray diffractometer (XRD, Bruker, USA) with Cu-Kα radiation of average wavelength 1.54059 Å. Their surface morphology was investigated using an Ultra Plus field-emission scanning electron microscope (FESEM, Zeiss, Germany) at 1 kV. The physical structure of powders was studied using a JEOL2100F field emission transmission electron microscope (TEM, JEOL, Japan) at 200 kV, and a CM 300 transmission electron microscope (TEM, FEI, USA) at 300 kV. The specific surface area of the particles was measured using the Brunauer-Emmett-Teller (BET) N_2-gas adsorption method in a TriStar 3020 instrument (Micromeritics, USA).

X-ray photoelectron spectroscopy (XPS) was conducted using a SPECS PHOIBOS 100 Analyser installed in a high-vacuum chamber with the base pressure below 8-10 mbar. X-ray excitation was provided by Al-Kα radiation with a photon energy of 1486.6 eV at a high voltage of 12 kV and a power of 144 W. XPS binding energy spectra were recorded at a pass energy of 20 eV and step widths of 0.05 - 0.1 eV in the fixed analyser transmission mode. To increase the signal/noise ratio, multi-scans were conducted and the intensity of signals were accumulated. Broad survey scans were recorded at a pass energy of 60 eV and a step width of 0.5 eV. XPS data analysis was carried out using the Casa XPS software package.

The bandgap energy was estimated from Tauc plots.[19] Band-edge positions were determined using a photocurrent onset technique.[20] An electrochemical cell was set up with oxide samples as a working electrode, platinum as a counter electrode, Ag/AgCl as a reference electrode and 0.1 M KCl solution as an electrolyte (bubbled with nitrogen gas for 3 h). Working electrodes were prepared by gradually dropping 4 ml of dispersed particles in ethanol (1 mg/mL), on a heated (200 °C) FTO glass surface (1.5 x 3 cm). Photo-electrochemical measurements were carried out using a potentiostat (Bio-Logic VMP3) and a set of light emitting diodes (220 V, 100 W), placed 10 cm away from the working electrode.

Preparation of electrodes in photo-electrochemical cells

Working electrodes were made by embedding the catalyst powders in a sub-micron thick film of polypyrrole (PPy) that was deposited on fluorine-doped tin-oxide (FTO) glass slides (Scheme 1a). PPy is a conductive polymer and was used to improve electronic conduction, to provide structural stability to the electrode by preventing photodegradation of the semiconductor, and to improve charge separation efficiency of the catalysts.[21] In addition, PPy generates charges upon visible light illumination and therefore nanoparticles modified with PPy have been shown to improve photocurrents.[22]

Prior to the deposition of electrode materials, FTO glass slides were first cleaned by sonicating (B2500R-MTH ultrasonic bath) in an acetone-filled chamber for 90 min, followed by washing with water and drying by blowing air over the slides. Organic contaminants were further removed using a DIG UV PSD PR SERIES digital ozone-UV cleaner for 20 min. Subsequently, the slides were cleaned in a PLASMAFLO PDC-FMG plasma cleaner, followed by drying using an IKA® RCT basic hotplate at 60 °C.

To prepare electrodes, iron(III) p-toluenesulfonate (Fe(III)-pTS) was used to assist in vapour phase polymerization of pyrrole.[23] First, 85 mg of Fe(III)-pTS (Sigma Aldrich) was dissolved in 1 mL ethanol and sonicated for 10 min. Subsequently, 8 mg of catalyst powder was added to the solution and sonicated for 1 h. The resulting solution (100 µL) was drop-cast onto the FTO glass slide and spun at 1500 revolutions per min (rpm) for 2 min using a WS-400B-6NPP/LITE spin-coater. The slide was kept on a hotplate and dried at 60 °C for 15 min.

Please do not adjust margins

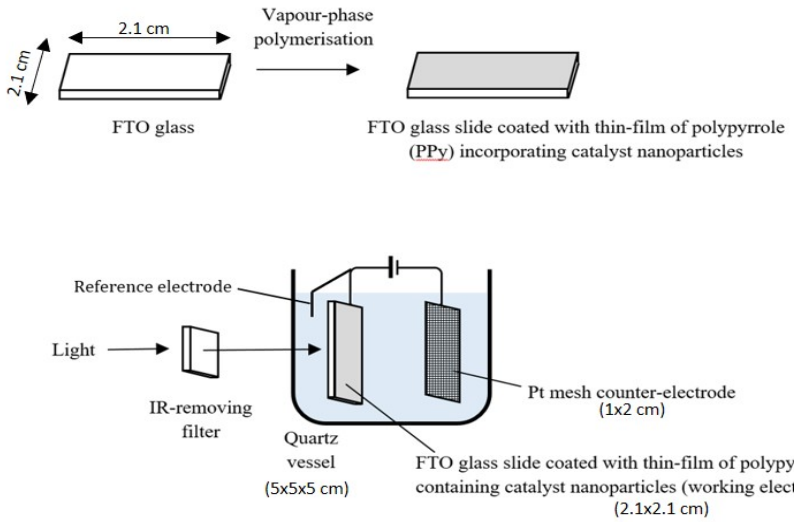

Scheme 1 Schematic depiction of: (a) the preparation of photoanodes for this study, (b) photoelectrochemical test cells of this study. Nanoparticles of amorphous or crystalline MnO_2, $Ca_2Mn_3O_8$, $CaMnO_3$ or $CaMn_2O_4$ ('catalysts') were incorporated into thin-films of polypyrrole (PPy) deposited on FTO glass slides. The coated glass slides were then studied as photoanodes that catalytically converted water into O_2. The calcium manganese oxide nanoparticles were structurally similar to the oxygen evolving centre (OEC) of photosynthesis.

Vapour phase polymerisation of pyrrole was carried out in a separate conical flask (500 mL capacity), equipped with a rubber stopper containing a crocodile clip. Within the flask, 0.500 mL pyrrole (Sigma Aldrich) was placed and the spin-coated FTO glass substrates were suspended above the pyrrole solution. The flask was placed in an oven at 60 °C for 25 min to allow polymerization of pyrrole on the slide surface. The sample was then washed with ethanol and dried. A copper wire was attached to the FTO surface with conductive silver paint and epoxy resin. Subsequently, the contact area of the wire was covered with epoxy glue. Control samples were also prepared without addition of catalytic particles.

OER photocatalysis study

The working electrodes (4.2 cm^2) were placed within a fully-enclosed quartz photoelectrochemical cell (5 x 5 x 5 cm) (Scheme 1(b)) inside a closed cabinet that comprised a Faraday cage. A Pt mesh (1 x 2 cm) and a BASi Ag/AgCl aqueous salt bridge (KCl, 3 M) were used as a counter electrode and a reference electrode, respectively. The cell was filled with a 0.2 M Na_2SO_4 aqueous solution electrolyte, adjusted to pH 12 by adding NaOH. Prior to experiment, the electrolyte was de-oxygenated by bubbling N_2 gas. Chronoamperograms (CA) were performed using an EDAQ466 potentiostat. Where applicable, the sample was illuminated with a SoLux daylight MR16 halogen light bulb (12 V, 50 W, 24°; ~0.25 sun intensity) with a stable output range of 275 - 750 nm. The light source was placed 10 cm from the working electrode and a Thorlabs visible-light bandpass filter (315-710 nm) was placed 1.5 cm in front of the light source to remove any infra-red wavelengths.

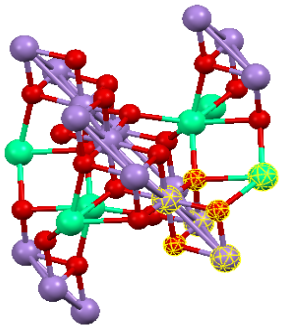

Fig. 2 Crystal structure of $Ca_2Mn_3O_8$. A section highlighted in yellow mesh, resembles the structure of natural water-oxidizing cubane. Ca is shown in green; Mn in blue; O in red.

Goodness of fit calculation

The local structures of $Ca_2Mn_3O_8$ and $CaMn_2O_4$ (Figs 2- 3) were quantitatively compared with that of the natural OEC cluster, by superimposition of their local atomic arrangements. The goodness-of-fit was calculated using a least-squares fitting method, in the following sequence.

First, the local structure of the natural OEC cubane, as shown in Fig. 1, was oriented in a Cartesian coordinate system in the following manner: The coordinate of the calcium atom was chosen to be (0,0,0). One of the oxygen atoms was placed on the x-axis, and the plane consisting of Ca1, O1 and O2 atoms (in Fig. 1) was adjusted to be on the x-y plane. Then, the coordinates of the rest of the atoms were calculated from the distance between two adjacent atoms, using the following equation:

This journal is © The Royal Society of Chemistry 20xx

Please do not adjust margins

$$D = \sqrt{(x_2 - x_1)^2 + (y_2 - y_1)^2 + (z_2 - z_1)^2} \quad (5)$$

where (x_1, y_1, z_1) and (x_2, y_2, z_2) are the Cartesian coordinates of adjacent two atoms. The distances between different atoms of the natural OEC cubane were taken from the literature.[2] Matlab was used to solve the set of equations created using the formula above.

Next, a section of the crystal structure, which resembles that of natural water-oxidizing cubane, was identified in the crystal structures of calcium manganese oxides. The selected local structure contained one calcium atom and three manganese atoms, as highlighted with yellow mesh in Fig. 2 for $Ca_2Mn_3O_8$ and Fig. 3 for $CaMn_2O_4$. The atomic coordinates in the selected local structure were collected from Materials Project, which is supported by the U.S. Department of Energy and provides computational data sets for various materials ($Ca_2Mn_3O_8$,[24] $CaMn_2O_4$[25]). The fractional coordinates obtained from Materials Project were converted into Cartesian coordinates. Using these coordinates, a section of the crystal structure was drawn using the "Mercury" software. With the help of the coordinates, distances between different atoms were calculated using Equation (5).

The calcium atom in the selected local structure was placed at the origin of the Cartesian coordinate system. The orientation of the selected local structure was defined with the rotational angles around x, y and z axes, Θx, Θy and Θz. After calculating the coordinates of all atoms as a function of Θx, Θy and Θz, goodness-of-fit was assessed by calculating the w-value using the following formula:

$$\omega^2 = \sum_i \left\{ (x_i - x_{ci})^2 + (y_i - y_{ci})^2 + (z_i - z_{ci})^2 \right\} \quad (6)$$

where (x_i, y_i, z_i) are the Cartesian coordinates of the i-th atom in the natural OEC cubane and (x_{ci}, y_{ci}, z_{ci}) are the coordinates of the corresponding atom in the selected local structure of calcium manganese oxides.

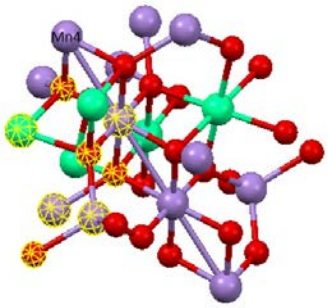

Fig. 3 Crystal structure of $CaMn_2O_4$. A section highlighted in yellow mesh, resembles the structure of natural OEC cubane. Calcium is sown in green;

Results and Discussions

Synthesis and Characterisation

Fig. 4(a) shows the XRD pattern of the amorphous MnO_2 powder after milling for 4h. In the pattern, predominant peaks corresponding to KCl (JCPDS # 73-0380) are visible due to the presence of excess KCl in the powder mixture. Fig. 4(b) shows

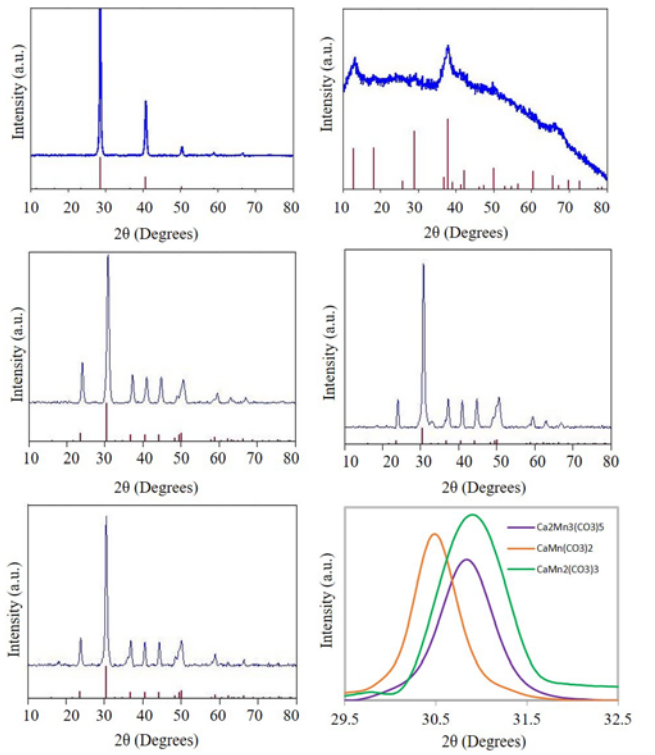

Fig. 4 XRD patterns of the as-milled powder of: (a) MnO_2 embedded in a KCl matrix (b) MnO_2 after removal of KCl, (c) washed $Ca_2Mn_3(CO_3)_8$ precursor, (d) washed $CaMn(CO_3)_2$ precursor, (e) washed $CaMn_2(CO_3)_3$ precursor, and (f) comparison of their highest diffraction peaks. The vertical lines at the bottom of (a-c) represent JCPDS data.

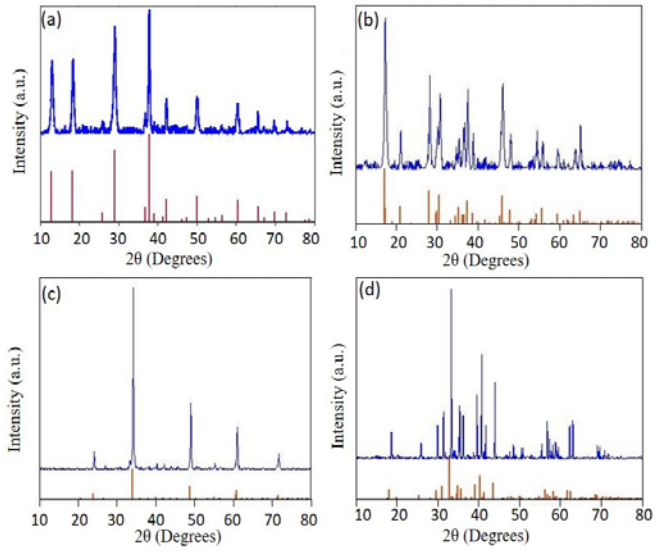

Fig. 5 XRD patterns of (a) MnO_2, (b) $Ca_2Mn_3O_8$, (c) $CaMnO_3$, and (d) $CaMn_2O_4$. The vertical lines at the bottom of (a-c) represent JCPDS data.

Please do not adjust margins

Please do not adjust margins

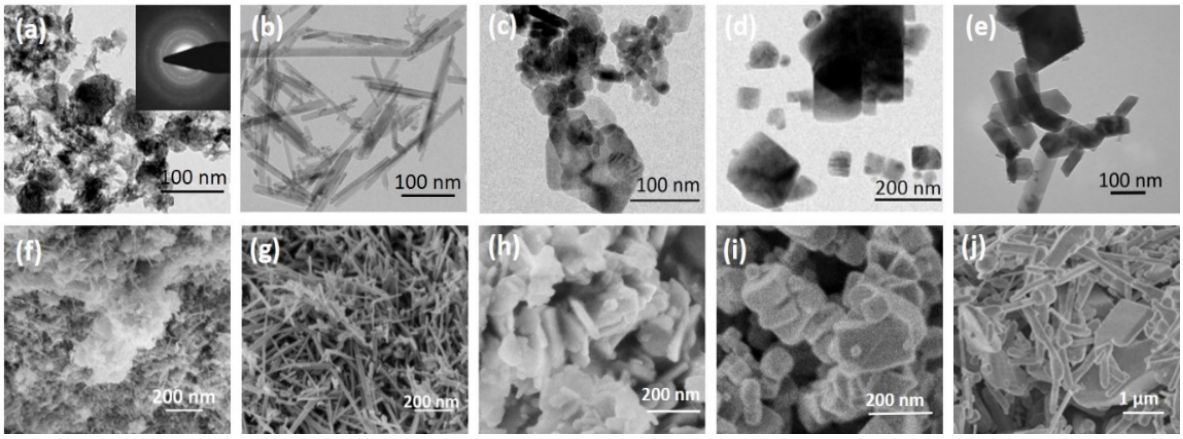

Fig. 6 TEM micrographs of (a) amorphous MnO_2, (b) crystalline MnO_2, (c) $Ca_2Mn_3O_8$, (d) $CaMnO_3$, and (e) $CaMn_2O_4$; high-resolution SEM micrographs of (f) amorphous MnO_2, (g) crystalline MnO_2, (h)$Ca_2Mn_3O_8$, (i) $CaMnO_3$, and (j) $CaMn_2O_4$. The inset in image (a) shows a selected area electron diffraction pattern of the same area.

the XRD pattern after washing to remove KCl, with two broad peaks near 13° and 37° and no other well-defined sharp peaks. This could be attributed to the amorphous nature of the powder. Figs 4(c)-4(e) show the XRD patterns of the CaMn carbonates (Equations (2)-(4)), after milling for 6 h and subsequent removal of the salt matrix phase The solid-state displacement reactions took place during milling, leading to the formation of $Ca_xMn_y(CO_3)_z$ (JCPDS # 84-1290). Fig. 4(f) shows that the positions of the highest diffraction peaks of $Ca_2Mn_3(CO_3)_5$, $CaMn_2(CO_3)_3$ and $CaMn(CO_3)_2$ differ slightly from each other, which could be attributed to different Mn/Ca ratios in the samples, due to the difference in ionic radii of Mn and Ca.[26]Figs 5(a)-5(d) show the XRD patterns of the powders after heat treatment and subsequent removal of the salt matrix phase. The diffraction peaks can be indexed to (a) MnO_2 (JCPDS # 72-1982), (b) $Ca_2Mn_3O_8$ (JCPDS # 73-2290), (c) $CaMnO_3$ (JCPDS # 89-0666) and (d) $CaMn_2O_4$ (JCPDS # 74-2293), respectively showing that the intended $Ca_xMn_yO_z$ phases were successfully formed.

Table 1 BET specific surface area

Catalyst	Specific surface area [m^2g^{-1}]
Amorphous MnO_2	204
Crystalline MnO_2	76
$Ca_2Mn_3O_8$	49
$CaMnO_3$	14
$CaMn_2O_4$	5

Table 2 Mn 2p3/2 and Mn 3s XPS data of as synthesized compounds.

Sample	Mn 2p3/2 (eV)	Mn 3s (eV) Peak 1	Mn 3s (eV) Peak 2	ΔEs (eV)	Average Oxidation State (AOS)[a]
Amorphous MnO_2	641.3	83.7	88.3	4.6	3.8
MnO_2 nanorods	641.8	84.1	88.5	4.4	4
$CaMnO_3$	641.8	83.8	88.2	4.4	4
$Ca_2Mn_3O_8$	642.3	84.1	88.4	4.3	4.1
$CaMn_2O_4$	640.8	84.1	89.3	5.2	3.1

[a] Calculated with the formula: AOS = 8.95–1.13 × ΔEs, where the ΔEs is the splitting energy of the Mn 3s.[28]

Figs 6(a) and 6(f) show TEM and SEM images of the as-milled and washed MnO_2 powder. The MnO_2 particles were mostly irregular-shaped, accompanied with a small number of needle-shaped particles with diameters less than 10 nm. The selected area electron diffraction pattern (inset in Fig. 6(a)) indicated a poorly crystalline nature of the MnO_2, which is in good agreement with the XRD data in Fig. 4(b). Needle-like structures could be the reason for the few spots observed on the diffraction rings. Figs 6(b) and 6(g) show typical TEM and SEM images of the MnO_2 powder after heat treatment. The sample consisted of only nanorods of about 15–20 nm in diameter with varying lengths. Figs 6(c) and 6(h) show TEM and SEM images of the $Ca_2Mn_3O_8$ nanoparticles. The particles were 30-100 nm in diameter with plate-like morphologies. In contrast, the $CaMnO_3$ particles had cuboidal shapes, with sizes ranging between 50 nm and 200 nm (Figs 6(d), 6(i))

Compared to the $Ca_2Mn_3O_8$ and $CaMnO_3$ particles made via direct calcination of a mixture of calcium and manganese carbonates reported in the literature,[26,] the $Ca_2Mn_3O_8$ and $CaMnO_3$ particles made via mechanochemical processing in this study were significantly smaller. However, the $CaMn_2O_4$ particles were irregular in shape with sizes from 200 nm to 2 µm as shown in Figs 6(e) and 6(j), due to the high temperature involved during synthesis.

The BET specific surface areas of the manganese oxide and calcium manganese oxide powders are listed in Table 1. The BET specific surface areas of $Ca_2Mn_3O_8$ and $CaMnO_3$ powders were 14 times and 5 times higher than that of $Ca_2Mn_3O_8$ and $CaMnO_3$ powders synthesised using ceramic methods.[7]This demonstrates the importance of mechanochemical method for high surface area catalyst synthesis.

XPS analysis was performed to characterize the surface oxidation states of the catalysts. Manganese oxidation is important for photoelectrochemical catalytic performance, which is discussed later in this paper. The results are shown in Fig. 7 and Table 2. Two intense peaks centred at approximately

This journal is © The Royal Society of Chemistry 20xx

Please do not adjust margins

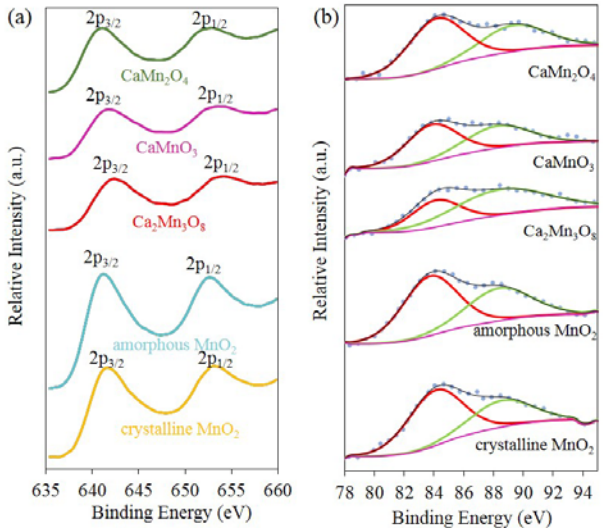

Fig.7 (a) Mn 2p and (b) Mn 3s XPS spectra of synthesized amorphous and crystalline MnO_2, $Ca_2Mn_3O_8$, $CaMnO_3$ and $CaMn_2O_4$.

641 eV and 653 eV were observed in the Mn 2p spectra, which were attributed to Mn $2p_{3/2}$ and Mn $2p_{1/2}$ spin-orbit doublet respectively (Fig. 7(a)). As shown in Table 2, the Mn $2p_{3/2}$ peak for $CaMn_2O_4$ was observed at a slightly lower binding energy due to the presence of Mn^{3+}. The Mn oxidation state could be qualitatively deduced from the chemical shift of the Mn 2p peak,[27] however a quantitative determination was not possible due to the small magnitude of the shift. Therefore, an average oxidation state (AOS) of the compounds, presented in Table 2, was calculated using the energy difference between the two 3s-manganese peaks (Fig. 7(b)).[28] AOS values obtained from the XPS analysis are in good agreement with the theoretical values of the oxidation states in these compounds. AOS for amorphous MnO_2 was found to be slightly lower than crystalline MnO_2, possibly due to the presence of surface oxygen vacancies and dangling bonds.

OER Photocatalysis

Fig. 8 shows the current densities at 1.00 V (vs Ag/AgCl), with and without light illumination. The working electrode, consisting of the oxide powder and PPy, produced higher dark and light currents, in comparison to a control working electrode comprising a thin-film of PPy alone on an FTO glass slide. Table 3 lists the average light and dark current densities exhibited by the different samples. The photoanodes containing $CaMnO_3$ and amorphous MnO_2 produced the highest 'dark' currents (without light illumination) and 'light' currents (with light illumination). The smallest dark current was produced by $CaMn_2O_4$/PPy, which, nevertheless, also yielded the largest photocurrent (i.e. the greatest difference between their light and dark current). The calcium-containing catalysts produced higher photocurrents than the MnO_2 ones.

Fig. 9 shows the Tauc plot in the form of $(\alpha h\nu)^2$ versus $h\nu$ for (a) amorphous MnO_2, (b) crystalline MnO_2, (c) $Ca_2Mn_3O_8$, (d) $CaMnO_3$ and (e) $CaMn_2O_4$, where h is the Planck's constant, ν is

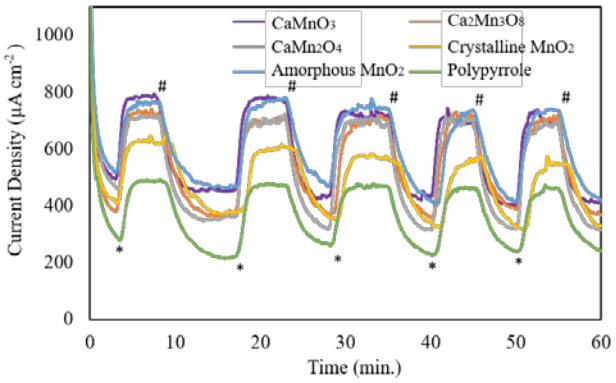

Fig. 8. Chronoamperograms at 1.00 V (vs Ag/AgCl) in 0.2 M Na_2SO_4 (pH 12) over 1 h of operation, with and without light illumination (0.25 sun), of FTO glass slides coated with thin films of amorphous and crystalline MnO_2, $Ca_2Mn_3O_8$, $CaMnO_3$, $CaMn_2O_4$ and polypyrrole (control). (*='light on', #='light off')

Table 3 Average light and dark current densities.

Sample	Average light current density (μA cm^{-2})	Average dark current density (μA cm^{-2})	Average photo current density (μA cm^{-2})
Amorphous MnO_2 / PPy	742	444	298
Crystalline MnO_2 / PPy	581	331	250
$CaMnO_3$ / PPy	746	440	306
$Ca_2Mn_3O_8$ / PPy	714	373	341
$CaMn_2O_4$ / PPy	701	326	375
PPy (control)	447	230	217

Table 4 Band gap, conduction and valence band edges of manganese-based oxides.

Sample	Band gap (eV)	Conduction band (eV)	Valence band (eV)
Amorphous MnO_2	2.54	0.83	3.37
Crystalline MnO_2	2.33	0.86	3.19
$CaMnO_3$	1.5	0.92	2.42
$Ca_2Mn_3O_8$	2.1	0.88	2.98
$CaMn_2O_4$	1.5	1.01	2.51
PPy	2.5	-0.47	2.03

the photon's frequency, and α is the absorption coefficient. Fig. 10 shows the photocurrent onset potential curves for (a) amorphous MnO_2, (b) crystalline MnO_2, (c) $Ca_2Mn_3O_8$, (d) $CaMnO_3$ and (e) $CaMn_2O_4$. Table 4 lists the optical band gaps, obtained from the Tauc plots, and edges of conduction and valence bands, estimated by the photocurrent onset method and band gap, respectively. The band gap and HOMO, LUMO levels of PPy were adopted from the literature.[29] Using the values in Table 4, a schematic diagram of the energy levels of the PPy/oxides electrodes is drawn in Fig. 11. PPy is itself a semiconductor that can absorb visible light to generate electrons and holes, and hence shows photocurrent generation as shown in Fig. 8. MnO_2 and CaMn oxides are also semiconductors that absorb visible light to generate electrons

Please do not adjust margins

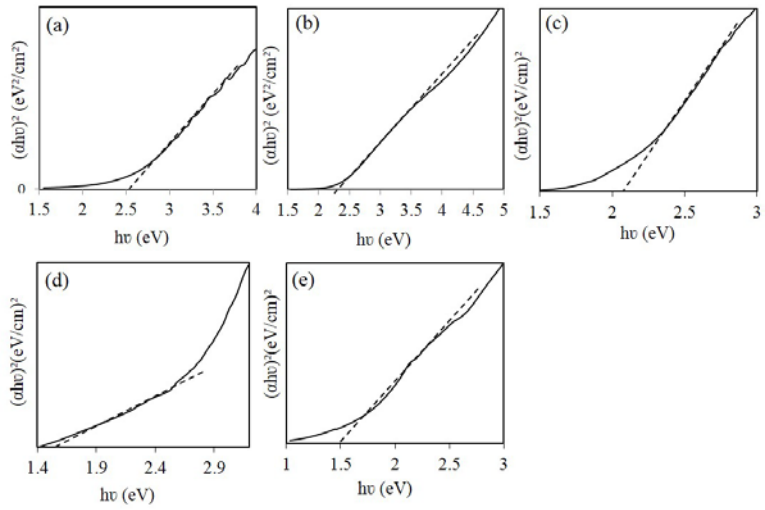

Fig. 9 Tauc plot for (a) amorphous MnO_2, (b) crystalline MnO_2, (c) $Ca_2Mn_3O_8$, (d) $CaMnO_3$ and (e) $CaMn_2O_4$

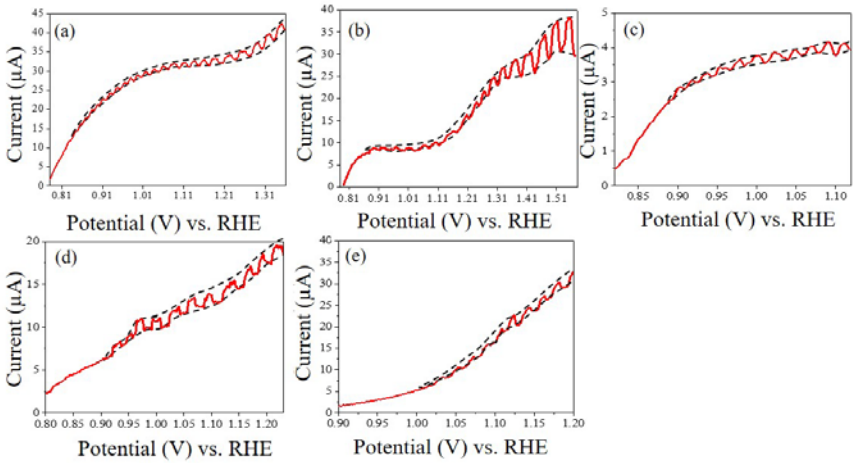

Fig. 10 Current potential curve (at 0.1 mV/s) of (a) amorphous MnO_2, (b) crystalline MnO_2, (c) $Ca_2Mn_3O_8$, (d) $CaMnO_3$ and (e) $CaMn_2O_4$ under chopped illumination.

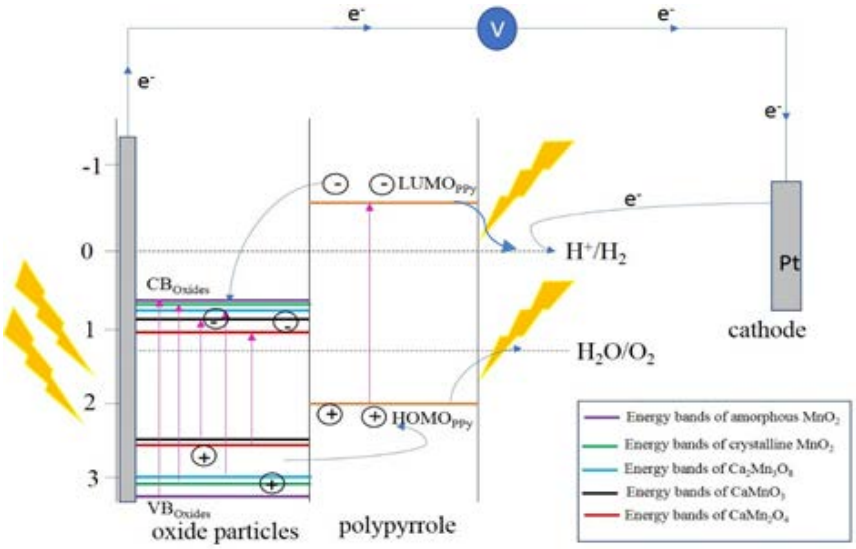

Fig. 11 Proposed mechanism depicted via a schematic diagram of the energy levels of the PPy-oxide particle electrodes.

This journal is © The Royal Society of Chemistry 20xx

Please do not adjust margins

(e^-) and holes (h^+), but their photocurrent without PPy was very small (Fig. 10). When the oxides and PPy were combined, a significant increase in current was observed (Fig. 8).

As shown in Fig. 11, PPy provides a pathway to prevent direct recombination of photo-generated holes and electrons, by forming a type-II (staggered type) heterojunction with the valence and conduction bands of the oxides. Since the valence band edges of oxide particles are more positive than the HOMO level of PPy, the holes photo-generated at the oxides are injected into the HOMO of PPy, which has sufficient electrochemical energy to produce oxygen from water via the following reaction:

$$2H_2O(l) + 4h^+ \rightarrow O_2(g) + 4H^+(aq) \quad (7)$$

The holes photo-generated at PPy also facilitate the production of O_2 from water. On the other hand, photo-excited electrons at PPy are either transferred to the conduction band of oxides and then to the FTO electrode to contribute to the photocurrent, or are used to generate hydrogen via the following reaction:

$$2H^+(aq) + 2e^- \rightarrow H_2(g) \quad (8)$$

Photo-excited electrons at the oxides can also contribute to the photocurrent but cannot be used to generate H_2 via the reaction (8), because their valence band edge energies are higher than the electrochemical potential of reaction (8).

Similarity in local atomic arrangement

Table 5. Calculated ω values for different orientations.

Compound	Orientation	ω value
$Ca_2Mn_3O_8$	1 (Figure 12b)	1.16
	2 (Figure 12c)	1.13
	3 (Figure 12d)	0.81
$CaMn_2O_4$	1 (Figure 13b)	2.77
	2 (Figure 13c)	2.65
	3 (Figure 13d)	2.61

In order to study the similarity of the local atomic arrangement of calcium manganates and the natural OER cubane, structural goodness-of-fit analysis was conducted.[30]

In the $Ca_2Mn_3O_8$ crystal, there is no manganese atom having a location equivalent to Mn4 in the natural OEC cubane (Fig. 1). Also, one oxygen is missing from the cube (Figs 12(b)-(d)). Therefore, for the structural goodness-of-fit analysis, there are three possible ways to orient the local structure of $Ca_2Mn_3O_8$ and $CaMn_2O_4$ to compare with that of the natural OEC cubane, as shown in Figs 12(b)-(d) and Figs 13(b)-(d), respectively. For comparison, the atomic configuration of the natural OEC cubane is also shown in Figs 12(a) and 13(a). In the crystal of $CaMn_2O_4$, there is a manganese atom having a location equivalent to Mn4 in the natural OEC cubane (Fig. 3). If the direction of Mn4 is matched in the two structures, there is only one way to orient the local structure of $CaMn_2O_4$ for the goodness-of-fit analysis (Fig. 13(c)). If the location of Mn4 is

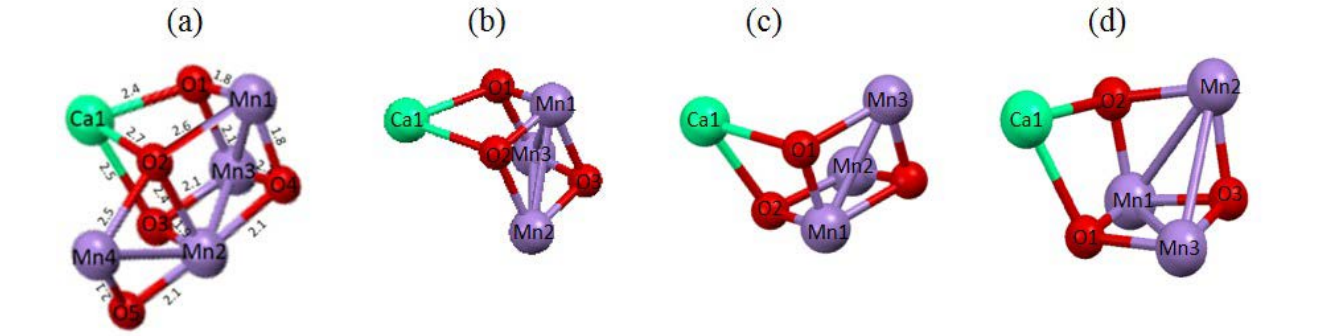

Fig. 12 Ball and stick model of (a) natural cubane, (b-d) three orientations of cubane-like part of $Ca_2Mn_3O_8$ crystal.

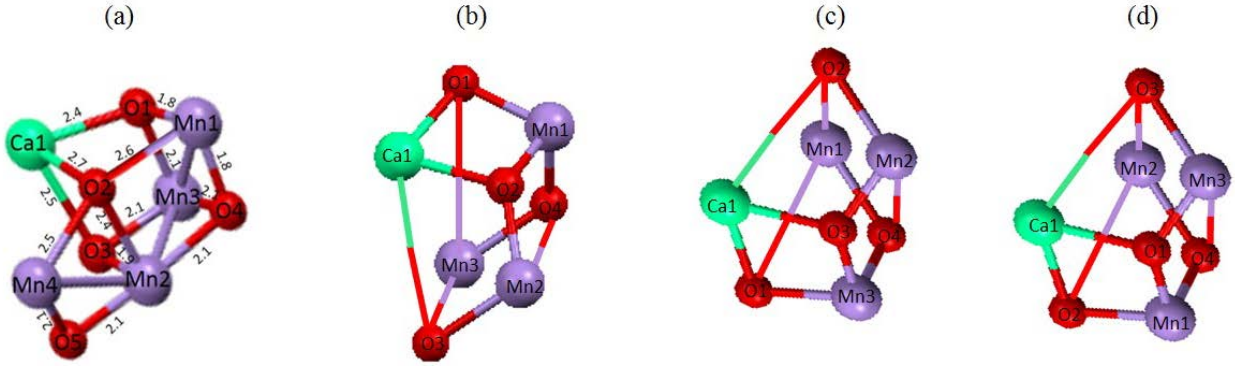

Fig. 13 Ball and stick model of (a) natural cubane, (b-d) three orientations of cubane-like part of $CaMn_2O_4$ crystal.

Please do not adjust margins

ignored, there are three possible ways to orient the local structure of $CaMn_2O_4$ as shown in Fig. 13(b)-(d). The structural goodness of fit was calculated for each orientation and expressed with ω as in Table 5. For $Ca_2Mn_3O_8$, the orientation in Fig. 12(d) gave much smaller ω values than other two orientations. For $CaMn_2O_4$, the ω values of the three orientations gave similar ω value but the orientation in Fig. 13(d) gave a slightly smaller ω value than the other two orientations. Overall $Ca_2Mn_3O_8$ gave significantly smaller ω values than $CaMn_2O_4$.

Overall comparison

In the past, studies of the catalytic activities of calcium manganates were motivated by their structural similarity to the natural OEC cubane. However, there are many factors that potentially affect the water oxidation activities of the oxide catalysts. The factors include specific surface area, light absorption efficiency (bandgap energy), charge separation efficiency and charge transfer efficiency, in addition to the oxidation state of manganese ions and the structural similarity to the natural OEC cubane.

In order to elucidate the effects of the oxidation state of manganese ions and the structural similarity to the natural OEC cubane, the photocurrent was converted to 'effective photocurrent', as shown in Table 6, where the effects of specific surface area, light absorption efficiency (bandgap energy) and charge separation efficiency are considered, using the following equation:

$$I_{eff} = I_{obs} / (S \cdot \eta_{charge} \cdot \eta_{abs}) \quad (9)$$

where I_{eff} is the effective photocurrent density, I_{obs} is the raw current density observed in μA· cm^{-2}, S is the specific surface area in $m^2 \cdot g^{-1}$, η_{charge} is the charge separation efficiency, and η_{abs} is the light harvesting efficiency of the catalyst powders. This approach may be somewhat simplistic but still provides insight into the potential causes of the difference in the photo-induced OER of the compounds.

Table 6 shows that, overall, all the CaMn oxides produced higher effective photocurrent than the Mn oxides. Although MnO_2 is one of the most studied photocatalysts among Mn-based materials, the present study showed that CaMn oxides are better photocatalysts than MnO_2. Under the dark condition, the research groups of Najafpour and Kurz[32] reported similar results in electrochemical water splitting; CaMn oxides produced higher water-oxidation efficiency than MnO_2. Wiechem *et al.* report that, when Ca is replaced by other alkali earth metals (Sr, Mg) in birnessites-type manganese oxides, the electrochemical water-oxidation activity decreased under the dark condition.[31] Based on their studies, Najafpour and Kurz argued the importance of Ca in the water-oxidation reaction, hypothesising that Ca will activate the O-O bond between water and oxide catalysts.[32] Rong *et al*. changed the Ca-to-Mn ratio in the birnessite structure and found that Ca-to-Mn ratio affects the efficiency of catalytic oxygen evolution reaction.[9]

Table 6. Effective photo current.

Sample	Effective photo current density	Mn oxidation state	Structural similarity to natural OEC
Amorphous MnO_2	0.078	3.8	No
Crystalline MnO_2	0.258	4	No
$CaMnO_3$	0.339	4	No
$Ca_2Mn_3O_8$	0.511	4.1	Yes (□=0.81)
$CaMn_2O_4$	1.478	3.1	Yes (□=2.77)

In the natural OEC cubane, Ca plays an essential role in water splitting.[33] Although the detailed structural and functional roles of Ca are still not fully understood, if Ca assists the interaction between water and the catalyst surface, the presence of Ca would be equally beneficial for water splitting under both light and dark conditions. However, the influence of the presence of Ca in the crystal structure of Mn-based catalysts should be considered in conjunction with other effects that the presence of Ca will bring to the materials, including the change in crystal structure that leads to the change in bandgap energy, band edge position, charge diffusion length and charge separation efficiency. Among the three CaMn oxides, the compounds with better structural similarity ($Ca_2Mn_3O_8$ and $CaMn_2O_4$) to the natural OEC cubane demonstrated higher effective photocurrent. Table 7 compares the local structure and manganese valence number of $Ca_2Mn_3O_8$ and $CaMn_2O_4$.

Although the structural similarity to the natural OEC cubane is higher for $Ca_2Mn_3O_8$ than $CaMn_2O_4$, $Ca_2Mn_3O_8$ showed lower effective photocurrent than $CaMn_2O_4$. One possible reason for the better structural goodness-of-fit of $Ca_2Mn_3O_8$ with the natural OEC than $CaMn_2O_4$, is the smaller number of atoms used for the goodness-of-fit calculation; an oxygen atom is absent from the cubane-like part of $Ca_2Mn_3O_8$ (Fig. 12), obviously rendering the possibility of less mismatch with the natural OEC.

On the other hand, the local crystal structure of $CaMn_2O_4$ has all the atoms at similar positions in the cubane. The results

Table 7 Comparison of $Ca_2Mn_3O_8$ and $CaMn_2O_4$.

Compound	Presence of manganese equivalent to Mn4 in OEC cubane	Bulk Mn valence number	Mn valence number	Goodness of fit (ω)	Photocatalysis
$Ca_2Mn_3O_8$	No	+4	4.1	0.81	lower than $CaMn_2O_4$
$CaMn_2O_4$	Yes	+3	3.1	2.77	higher than $Ca_2Mn_3O_8$

This journal is © The Royal Society of Chemistry 20xx

Please do not adjust margins

Please do not adjust margins

can be interpreted as that, having all atoms in the cubane-like structure may be more important than having close geometry to the natural OEC. In addition, the presence of Mn4 and/or the oxidation state of Mn may be more important than the actual shape of the cubane-like part of the crystal structure. In fact, in the natural OEC cubane, the fourth manganese ion plays a key role in the water-splitting process and the three other manganese in the cube act as hole donors to the fourth manganese.[3,34]

Han *et al*.[26] and Zaharieva *et al*.[35] reported similar observations in electrochemical water splitting under dark conditions; the compounds with better structural similarity ($Ca_2Mn_3O_8$ and $CaMn_2O_4$) to the natural OEC cubane demonstrated higher effective current. It is tempting to speculate that a structural role similar to that in the natural OEC cubane is present in the ceramic calcium manganates. However, the influence of the local crystal structure of manganese-based catalysts on photocurrent should be carefully considered in conjunction with other effects that the local atomic structure will introduce to the materials, including the change in bandgap energy, band edge position, charge diffusion length and charge separation efficiency, which is lacking in the past studies.

In Table 6, it is evident that crystalline MnO_2 showed higher effective photocurrent than amorphous MnO_2. From the results, it may be speculated that a higher Mn oxidation state may be favorable for photocatalytic water splitting. Experimental and computational studies conducted on Mn oxidation states in the natural OEC cubane also support the high valent oxidation scheme.[36-38] However, $CaMn_2O_4$ showed the highest effective photocurrent, despite having the lowest Mn oxidation state among all the compounds studied in the present work. Therefore, it is not conclusive whether and to what extent the oxidation states of Mn influences the photo-induced water oxidation catalysis. The results of previous studies under dark conditions in electrochemical water oxidation (i.e. non-photocatalytic) are also inconclusive in this respect. Frey *et al*. reported that Ca manganates with higher oxidation states of Mn gave higher catalytic performance in the dark,[6] whereas Rong *et al*. [9] and Baktash *et al*. [5] reported that intermediate oxidation states of Mn between 3.5 and 4 are most active in water oxidation in the dark. It is prudent to point out that these discussions of the effect of Mn oxidation states in water oxidation catalysis did not consider the overall effects of the change in the oxidation states, including the creation of intra-bandgap defect energy levels and charge separation efficiency.

In addition, Pokhrel *et al.*[39] made an interesting observation that water oxidation abilities are dependent on the test conditions. They tested nine crystalline MnO_x materials (α-MnO_2, β-MnO_2, R-MnO_2, λ-MnO_2, δ-MnO_2, γ-MnO_2, Mn_2O_3, Mn_3O_4, $LiMn_2O_4$) by chemical, photochemical and electrochemical assays, and reported that the identity of the "best" catalysis is dependent on the oxidation method. Their results showed that γ-MnO_2 performed the best in a ceric ammonium nitrate solution of pH 0.8 (chemical oxidant method), Mn_2O_3 showed highest water oxidation during photochemical assay (pH 8) and the best catalysts was dependent on the pH of electrolyte during electrochemical testing which was Mn_2O_3 (for acidic electrolyte), γ-MnO_2 (for neutral pH electrolyte) and α-MnO_2 (for alkaline electrolyte).[39] Thus, it could be concluded that water splitting abilities of the different oxidation state of manganese are also strongly dependent on experimental conditions.

Overall, our study suggests that, for the development of manganese-based water oxidation photocatalysts, there may be some possible importance of having a local structure similar to that of the natural OEC cubane including the presence of Ca, but it also highlights the danger in taking a simplistic approach by focusing on the local structure only. Other factors such as those noted above may also influence catalytic performance and these need to be taken into account when seeking to design a bio-mimetic moiety.

Conclusions

In the present study, different CaMn oxides ($CaMnO_3$, $Ca_2Mn_3O_8$ and $CaMn_2O_4$) were investigated for their catalytic properties in photo-electrochemical water oxidation, in a photo-electrochemical cell, for the first time. Mn oxides (amorphous MnO_2 and crystalline MnO_2) were also studied for comparison. The results demonstrated that the electrode films containing oxide powders produced higher dark and light currents relative to the film without the oxides. The highest photocurrent was observed for the anode containing $CaMn_2O_4$. It was found that the band edges of CaMn oxides are suitable for oxygen evolution through water splitting. Although MnO_2 has been known as one of the most promising redox catalysts and photocatalysts among Mn-based materials, the present study showed that CaMn oxides can induce higher photocurrents than MnO_2, at least around pH 12. Hence this study signifies the importance of further research on calcium manganate ceramics as a new class of catalysts in photo-electrochemical water splitting.

The present study also demonstrated the effectiveness of a new anode design for Mn-based catalysts in photo-electrochemical cells. The catalyst materials were embedded within PPy to form an anode, which enabled high conductivity and catalytic turnover within the anode. The combination of CaMn oxides and PPy formed a type-II (staggered type) heterojunction, enabling increased charge separation efficiency within the anode and, in turn, improved oxygen evolution in the photo-electrochemical cell. The optimisation of the anode design including powder loading and thickness was outside the scope of this investigation and is subject to further studies.

In the past, studies of the catalytic activities of calcium manganates was motivated by their structural similarity to the natural OEC cubane. However, the present study signals that much caution is required to this approach. Quantitative structural goodness-of-fit studies revealed that, although the structural similarity to the natural OEC cubane is higher for $Ca_2Mn_3O_8$ than $CaMn_2O_4$, $Ca_2Mn_3O_8$ showed lower effective photocurrent than $CaMn_2O_4$. The results imply that it is important to carefully consider the role of other factors that potentially affect the water oxidation activities of the oxide catalysts, such as Mn oxidation states, presence of crystal

Please do not adjust margins

Please do not adjust margins

defects, electron energy states (bandgap energy & band edge positions) and experimental conditions, to conduct an overall assessment of the catalytic activities of calcium manganates. The discussions made in the scientific literature should be critically interpreted accordingly. Although the detailed mechanism should be further discussed over the experimental data of turnover number, turnover frequency and oxygen yield, the present work provides important information for future studies to develop a better design of biomimetic photocatalysts.

Conflicts of interest

There are no conflicts to declare.

Acknowledgements

AG would like to recognize a PhD research fellowship from the Australian National University. Access to the facilities of the Centre for Advanced Microscopy (CAM) with funding through the Australian Microscopy and Microanalysis Research Facility (AMMRF) is gratefully acknowledged. MA thanks the Government of Iraq for a PhD scholarship. All authors thank A/Prof Attila Mozer of the University of Wollongong for use of a GC gas analyser. The authors are grateful to Dr. Michael Cheah and Paul Carr of the Australian National University for critical discussions. The authors also acknowledge the Australian National Fabrication Facility (ANFF) Materials Node for equipment use and Mr Adam Taylor for design and printing of the custom-built apparatus. Support from the Australian Research Council Centre of Excellence for Electromaterials Science (Grant Number CE140100012) is gratefully acknowledged.

References

1 M.M. Najafpour, *J. Photochem. Photobiol. B, Biol.*, 2011, **104**, 111-117.
2 Y. Umena, K. Kawakami, J.R. Shen and N. Kamiya, *Nature*, 2011, **473**, 55.
3 J. Barber, *Biochem.*, 2016, **55**, 5901-5906.
4 A. Gagrani and T. Tsuzuki, *Chem. Eng. Sci*., 2019, **194**, 116-126.
5 E. Baktash, I. Zaharieva, M. Schröder, C. Goebel, H. Dau, and A. Thomas, *Dalton Trans*., 2013, **42**, 16920-16929.
6 C.E. Frey, M. Wiechen and P. Kurz, *Dalton Trans.*, 2014, **43**, 4370-4379.
7 M.M. Najafpour, B. Pashaei and S. Nayeri, *Dalton Trans*., 2012, **41**, 4799-4805.
8 A.R. Parent, R.H. Crabtree and G.W. Brudvig., *Chem. Soc. Rev.*, 2013, **42**, 2247-2252.
9 F. Rong, J. Zhao, Z. Chen, Y. Xu, Y. Zhao, Q. Yang and C. Li, *J. Mater. Chem. A*, 2016, **4**, 6585-6594.
10 Z.N. Zahran, E.A. Mohamed and Y. Naruta, *J. Mater. Chem. A*, 2017, **5**, 15167-15174.
11 A. Ramírez, P. Bogdanoff, D. Friedrich and S. Fiechter, *Nano Energy*, 2012, **1**, 282-289.
12 J. Du, T. Zhang, F. Cheng, W. Chu, Z. Wu and J. Chen, *Inorg. Chem.*, 2014, **53**, 9106-9114.
13 S. Raabe, D. Mierwaldt, J. Ciston, M. Uijttewaal, H. Stein, J. Hoffmann, Y. Zhu, P. Blöchl C. Jooss, C., *Adv. Funct. Mater.*, 2012, **22**, 3378-3388.
14 S.Y. Lee, D. González-Flores, J. Ohms, T. Trost, H. Dau, I. Zaharieva and P. Kurz, *ChemSusChem*, 2014, **7**, 3442-3451.
15 M.M. Najafpour, *Dalton Trans.*, 2011, **40**, 3793-3795.
16 M.M. Najafpour and D.J. Sedigh, *Dalton Trans.*, 2013, **42**, 12173-12178
17 A. Gagrani, J. Zhou and T. Tsuzuki, *Ceram. Int.*, 2018, **44**, 4694-4698.
18 S. Sinha, N. Deshpande and D. Deshpande, *Thermochim. Acta*, 1987, **113**, 95-104.
19 B.D. Viezbicke, S. Patel, B.E. Davis and D.P. Birnie, *Physica Status Solidi B*, 2015, **252**, 1700-1710.
20 B.A. Pinaud, Z. Chen, D.N. Abram and T.F. Jaramillo, *J. Phys. Chem. C*, 2011, **115**, 11830-11838.
21 A.J. Frank and K. Honda, *J. Photochem.*, 1985, **29**, 195-204.
22 Z. Zhang, Y. Yuan, L. Liang, Y. Cheng, H. Xu, G. Shi and L. Jin, *Thin Solid Films*, 2008, **516**, 8663-8667.
23 B. Winther-Jensen, J. Chen, K. West and G. Wallace, *Macromol.*, 2004, **37**, 5930-5935.
24 https://materialsproject.org/materials/mp-18893/#, viewed 20 July 2017.
25 https://materialsproject.org/materials/mvc-6593/#, viewed 20 July 2017.
26 X. Han, T. Zhang, J. Du, F. Cheng and J. Chen, *Chem. Sci.*, 2013, **4**, pp.368-376.
27 M.M. Jorge, A.C. dos Santos and M.R. Nunes, *Int. J. Inorg. Mater.*, 2001, **3**, 915-921.
28 M. Sun, B. Zhang, H. Liu, B. He, F. Ye, L. Yu, C. Sun, and H. Wen, *RCS Adv.*, 2017, **7**, 3958-3965.
29 J. Wang and X. Ni, *Solid State Commun.*, 2008, **146**, 239-244.
30 G.F. Swiegers, J.K. Clegg and R. Stranger, *Chem. Sci.*, 2011, **2**, 2254-2262.
31 M. Wiechen, I. Zaharieva, H. Dau and P. Kurz, *Chem. Sci.*, 2012, **3**, 2330-2339.
32 M.M. Najafpour, T. Ehrenberg, M. Wiechen and P. Kurz, *Angewandte Chemie Int. Ed.*, 2010, **49**, 2233-2237.
33 C.F. Yocum, *Coord. Chem. Rev.*, 2008, **252**, 296-305.
34 J. Barber, *Chem. Soc. Rev.*, 2009, **38**,185-196.
35 I. Zaharieva, M.M. Najafpour, M. Wiechen, M. Haumann, P. Kurz and H. Dau, *Energy Environ. Sci.*, 2011, **4**, 2400-2408.
36 J. Messinger, J.H. Robblee, U. Bergmann, C. Fernandez, P. Glatzel, H. Visser, R.M. Cinco, K.L. McFarlane, E. Bellacchio, S.A. Pizarro and S.P. Cramer, *J. Am. Chem. Soc.*, 2001, **123**, 7804-7820.
37 L. Iuzzolino, J. Dittmer, W. Dörner, W. Meyer-Klaucke and H. Dau, *Biochem.*, 1998, **37**, 17112-17119.
38 V. Krewald, M. Retegan, N. Cox, J. Messinger, W. Lubitz, S. DeBeer, F. Neese and D.A. Pantazis, *Chem. Sci.*, 2015, **6**, 1676-1695.
39 R. Pokhrel, M.K. Goetz, S.E. Shaner, X. Wu and S.S. Stahl, *J. Am. Chem. Soc.*, 2015, **137**, 8384-8387.

 This journal is © The Royal Society of Chemistry 20xx

Please do not adjust margins